Available at www.ComputerScienceWeb.com
POWERED BY SCIENCE DIRECT®

Medical Image Analysis 7 (2003) 435–444

MEDICAL IMAGE ANALYSIS
www.elsevier.com/locate/media

In vivo strain and stress estimation of the heart left and right ventricles from MRI images☆

Zhenhua Hu[a], Dimitris Metaxas[b,*], Leon Axel[c]

[a]Department of Computer and Information Science, University of Pennsylvania, Levine Hall, 3330 Walnut Street, Philadelphia, PA 19104, USA
[b]The Center of Computational Biomedicine, Imaging and Modeling, Rutgers University, New Brunswick, NJ 08854-8019, USA
[c]Department of Radiology, New York University, 650 First Avenue, Room 600-A, 6th Floor, New York, NY 10016, USA

Abstract

Mechanical properties of the myocardium have been investigated intensively in the last four decades. Many complex strain energy functions have been used to estimate the stress–strain relationship of myocardium because the heart muscle is an inhomogeneous, anisotropic, and nearly incompressible material, which undergoes large deformations. These functions can be effective for fitting in vitro experimental data from myocardial stretch testing. However, it is difficult to model in vivo myocardium using these strain energy functions. Moreover, such estimates have so far been carried out almost exclusively on the left ventricle, because of the relative thinness and complex geometry of the right ventricle. Previous work from our research group has successful estimated the motion and deformation of both the left and the right ventricles, using data from noninvasive tagged magnetic resonance imaging. In this paper, we present a novel statistical model to estimate the in vivo material properties and strain and stress distribution in both ventricles, using such data. Two normal hearts and two hearts with right-ventricular hypertrophy (RVH) were studied and noticeable differences were found between the strain and stress distributions for normal volunteers and RVH patients. Compared to the strain energy function approach, our model is more intuitively understandable.

Keywords: Heart ventricle; Strain–stress; MRI tagging; EM algorithm; Composite material model

1. Introduction

To better understand cardiac diseases, we need more information about cardiac motion. Stress and strain of the heart are two of the most important determinants of many cardiac physiological and pathophysiological functions, including: (1) the pumping performance of the ventricle; (2) the oxygen demand of the myocardium; (3) the distribution of coronary blood flow; (4) the vulnerability of regions to ischemia and infarction; (5) the stimuli to growth and remodeling during development and disease; and (6) the risk of arrhythmia (Glass et al., 1991). Stress and strain in the heart wall depend on not only the structure and material properties of the heart but also the active force generated by the heart muscle and the effects of the intracavitary blood pressure on the heart wall.

The heart wall consists primarily of locally parallel muscle cells, a complex vascular network, and a dense plexus of connective tissue (Glass et al., 1991). The cardiac muscle cell is the predominant component of myocardium, normally occupying around 70% of heart wall volume. The muscle cells are tied together by a collagenous network and bundled together into fibers. There are two major groups of myocardial collagen (Caulfield and Borg, 1979): one group provides myocyte-to-myocyte and myocyte-to-capillary connections, while another group surrounds the muscle fibers. Systematic measurements of muscle fiber orientations of canine heart were carried out by Streeter and Hanna (1973). He found that fiber directions generally vary in a continuous manner from $+60°$ on the endocardium to $-60°$ on the epicardium. Other studies have shown similar transmural fiber orientation distribution in other mammalian species.

The material properties of heart wall were initially

☆Supplementary data associated with this article can be found at doi:10.1016/S1361-8415(03)00032-X

*Corresponding author.
E-mail addresses: zhhu@seas.upenn.edu (Z. Hu), dnm@cs.rutgers.edu (D. Metaxas), leon.axel@med.nyu.edu (L. Axel).

1361-8415/03/$ – see front matter
doi:10.1016/S1361-8415(03)00032-X

estimated based on uniaxial tests, mostly performed with papillary muscles (Pinto and Fung, 1973; Pao et al., 1980). Biaxial tests were subsequently carried out (Demer and Yin, 1983; Yin et al., 1987), showing that the myocardium is anisotropic; corresponding anisotropic constitutive relations have been proposed (Humphrey and Yin, 1987, 1989). Different complex forms of strain energy function have been used to model the material properties of the heart wall by fitting the experimental data from excised tissue (Glass et al., 1991). However, it is difficult to understand the real meaning of the parameters in these strain energy functions since they do not offer us a direct quantitative relation between stress and strain. The structure of myocardium reveals that it is a composite material. As an alternative approach, we can use a fiber-reinforced composite material model for the stress estimation of the in vivo left and right ventricles. By using this composite material model, we can estimate parameters such as Young's modulus and the Poisson ratio, which are more understandable and intuitively meaningful than the strain energy function parameters.

The active force was modeled in (Usyk et al., 2000) and the blood pressure has been described in many sources, such as (Guyton and Hall, 2000). Recently, experiments have been carried out on in vitro left ventricle strain and stress (Costa, 1996). However, the stress and strain estimation of the in vivo heart is much more complicated than that of the in vitro heart. This is because any invasive method will change the heart material properties and the local stress distribution, and it is not yet possible to measure the heart properties and the active force noninvasively. Some other researchers have estimated the in vivo strain of the left ventricle by using echocardiography (Papademetris et al., 2001; Papademetris, 2000). However, the echocardiographic image is not capable of showing the motion within the heart wall. The magnetic resonance imaging (MRI) tissue tagging technique (Axel and Dougherty, 1989; Young et al., 1993) provides an effective means to estimate the heart wall motion noninvasively. The MRI tissue tagging makes it possible to track material points within the heart wall and it does not change the material properties or motion of the heart tissue.

In this paper, the displacements of a bi-ventricular model of myocardium were reconstructed from MRI-SPAMM tagging and a physics-based deformable model method (Metaxas, 1996) based on previous work of Haber (Haber, 2000; Haber et al., 2000). Based on the motion data reconstructed from MRI tagging (Park et al., 1996; Haber et al., 2000) and the previously measured in vitro material properties (Usyk et al., 2000), we have estimated the active force. Using the estimated active force, we have estimated the in vivo material properties. Iterating these calculations, we can get the maximum likelihood estimation of the active force and the material properties. The finite element method (Bathe, 1982) was used to calculate the strain and stress. We studied the heart contraction cycle from the end of diastole to the end of systole. The previously measured fiber orientation data from animal hearts is applied in our heart model at the end of diastole. The fiber moves along with the heart wall in which it is embedded, and its orientation changes at every time step during the heart contraction cycle. Assuming the fiber's local material coordinates are constant, we can calculate the spatial coordinates of representative points on the fiber at each time step and then compute the current fiber orientation. The heart muscle stiffness is simplified as piece-wise linear and the Young's modulus depends on how much the muscle has deformed. It has been shown that residual stress exists in the left ventricle (Fung, 1984; Omens, 1988; Omens and Fung, 1990a,b), which reduces the endocardial stress concentrations during diastole. We applied the residual stress at the end of diastole to make our model more realistic. The principal boundary condition in our model is the blood pressure in the ventricular cavities.

2. Mechanical model

2.1. Geometrical model

The geometrical model chosen is the same as given in (Haber et al., 2000; Haber, 2000). The fiber orientation is based on data from other researchers (Nielsen et al., 1991; Vetter and McCulloch, 1998). The schematic fiber orientation on the epicardium of LV is shown in Fig. 1.

2.2. Composite material model

A composite is a structural material which consists of two or more constituents, which are combined at a macroscopic level and are not soluble in each other (Kaw, 1997). One constituent is called the reinforcing phase, which is embedded in another constituent called the matrix. In our model, the reinforcing phase is muscle fiber and the matrix is collagen.

Consider a representative volume element from a unidirectional lamina which consists of the fiber surrounded

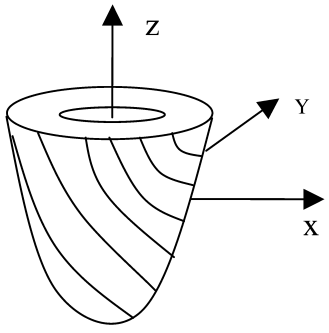

Fig. 1. Schematic fiber orientation on LV epicardium.

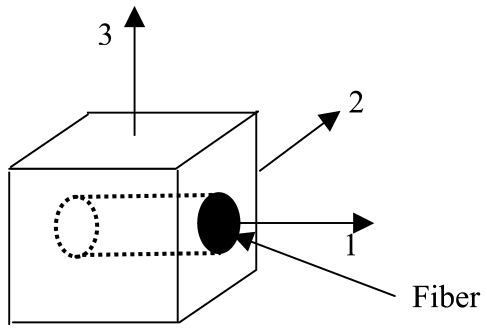

Fig. 2. Elastic moduli evaluation of the composite.

by the matrix (Fig. 2). Assume the fiber and matrix volume fractions are V_f and V_m, respectively, the Young's moduli of the fiber and matrix are E_f and E_m, respectively, the Poisson ratios are υ_f and υ_m, respectively, and the in-plane shear moduli are G_f and G_m, respectively. For the composite, the Young's moduli along the fiber orientation and across the fibers are, respectively (Kaw, 1997)

$$E_1 = E_f V_f + E_m V_m$$
$$E_2 = \left(\frac{V_f}{E_f} + \frac{V_m}{E_m}\right)^{-1}. \quad (1)$$

The Poisson ratio and the in-plane shear modulus are, respectively (Kaw, 1997):

$$\upsilon_{12} = \upsilon_f V_f + \upsilon_m V_m$$
$$G_{12} = \left(\frac{V_f}{G_f} + \frac{V_m}{G_m}\right)^{-1}. \quad (2)$$

The stress–strain relation is given by (Hyer, 1998)

$$\varepsilon = \begin{bmatrix} 1/E_1 & -\nu_{12}/E_1 & -\nu_{12}/E_1 & 0 & 0 & 0 \\ -\nu_{12}/E_1 & 1/E_2 & -\nu_{23}/E_2 & 0 & 0 & 0 \\ -\nu_{12}/E_1 & -\nu_{23}/E_2 & 1/E_2 & 0 & 0 & 0 \\ 0 & 0 & 0 & 2(1+\nu_{23})/E_2 & 0 & 0 \\ 0 & 0 & 0 & 0 & 1/G_{12} & 0 \\ 0 & 0 & 0 & 0 & 0 & 1/G_{12} \end{bmatrix} \sigma = C\,\sigma, \quad (3)$$

where E_1 is the Young's modulus along the fiber direction, E_2 is the Young's modulus along the cross-fiber direction, ν_{12} and ν_{23} are the corresponding Poisson ratios, and G_{12} is the shear modulus. Since the stress–strain relation of myocardium is nonlinear, both Young's moduli are assumed piece-wise linear. The piece-wise linearity can approximate the nonlinearity perfectly if each piece is infinitesimal. However, due to temporal resolution limitation of MRI, four linear elasticity intervals are used to approximate the stress–strain relation in myocardium as shown qualitatively in Fig. 3. Poisson ratios are assumed to be 0.4 since myocardium is approximately incompressible (Amini et al., 1998); the lock of full incompressibility can be included in the model. G_{12} is assumed to be equal to $E_2/(1+\upsilon_{23})$. C is called the compliance matrix.

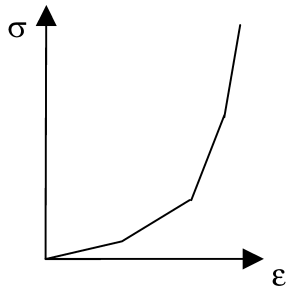

Fig. 3. Piece-wise linearity of Young's modulus.

2.3. Coordinate transformation relation

The stress–strain relationship in Eq. (3) is defined with respect to local material coordinates. Since the fiber orientation varies in different regions of the left ventricle (Caulfield and Borg, 1979), we need to transform the local stress–strain relation into a global stress–strain relation when implementing the finite element method. For the coordinates shown in Fig. 4, the stress in local fiber coordinates (1,2,3) can be transformed into global element coordinates (x,y,z) by (Hyer, 1998)

$$\sigma_{123} = \begin{bmatrix} \sigma_1 \\ \sigma_2 \\ \sigma_3 \\ \tau_{23} \\ \tau_{31} \\ \tau_{12} \end{bmatrix} = \begin{bmatrix} \cos^2\theta & \sin^2\theta & 0 & 0 & 0 & 2\sin\theta\cos\theta \\ \sin^2\theta & \cos^2\theta & 0 & 0 & 0 & -2\sin\theta\cos\theta \\ 0 & 0 & 1 & 0 & 0 & 0 \\ 0 & 0 & 0 & \cos\theta & -\sin\theta & 0 \\ 0 & 0 & 0 & \sin\theta & \cos\theta & 0 \\ -\sin\theta\cos\theta & \sin\theta\cos\theta & 0 & 0 & 0 & \cos^2\theta - \sin^2\theta \end{bmatrix} \begin{bmatrix} \sigma_x \\ \sigma_y \\ \sigma_z \\ \tau_{yx} \\ \tau_{zx} \\ \tau_{xy} \end{bmatrix} = T\sigma_{xyz}. \quad (4)$$

The strain transformation can be expressed in tensor form as

$$\varepsilon_{123} = T\varepsilon_{xyz}. \quad (5)$$

By inverting Eqs. (4) and (5) and combining with Eq. (3),

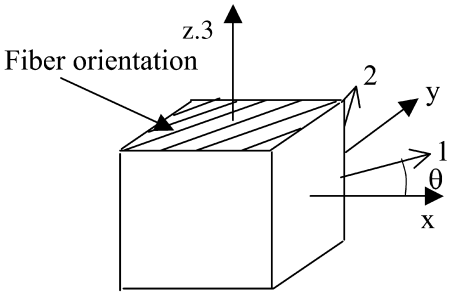

Fig. 4. Coordinate transformation.

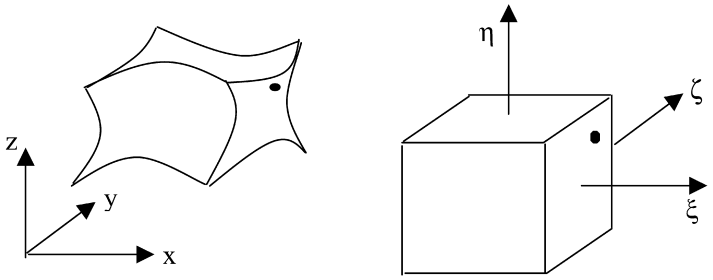

Fig. 5. Isoparametric Finite Element: one irregular element is mapped into one regular element, the black dot on the left image is an arbitrary point on one surface of the irregular element, its corresponding point is shown on the right image.

we have the stress–strain relation represented in global coordinates x–y–z as:

$$\varepsilon_{xyz} = T^{-1}CT\sigma_{xyz} = C_1\sigma_{xyz}. \tag{6}$$

3. Finite element method

3.1. Model dynamics

The finite element equation is derived by using energy minimization and the variational formulation (Bathe, 1982):

$$\frac{\mathrm{d}q}{\mathrm{d}t} + K(q - q_0) = P, \tag{7}$$

where q represents the displacement, q_0 represents the displacement generated by residual strain, K is the stiffness matrix, and P is the load vector. K and P can be calculated as

$$\begin{aligned} K &= \sum_e \left(\int_{V^e} B^{\mathrm{T}} D B \, \mathrm{d}V \right) \\ P &= P_{\mathrm{p}} + P_{\mathrm{a}} = \sum_e \left(\int_{S^e} N^{\mathrm{T}} f_{\mathrm{p}} \, \mathrm{d}S + \int_{V^e} N^{\mathrm{T}} f_{\mathrm{a}} \, \mathrm{d}V \right), \end{aligned} \tag{8}$$

where f_{p} is the boundary force (mainly generated by the pressure of the blood in the cavity), and f_{a} is the active force generated by the fiber. D is the elasticity matrix; it is the inverse of the compliance matrix given in Eq. (3). B is the strain–displacement matrix that relates nodal strain, ε, to nodal displacements, q, as $\varepsilon = Bq$. For an eight-noded element, B is as follows:

$$B = [B_1 \quad B_2 \quad B_3 \quad B_4 \quad B_5 \quad B_6 \quad B_7 \quad B_8], \tag{9}$$

where each sub-matrix B_i ($i = 1, \ldots, 8$) is as follows:

$$B_i = \begin{bmatrix} \frac{\partial N_i}{\partial x} & 0 & 0 \\ 0 & \frac{\partial N_i}{\partial y} & 0 \\ 0 & 0 & \frac{\partial N_i}{\partial z} \\ 0 & \frac{\partial N_i}{\partial z} & \frac{\partial N_i}{\partial y} \\ \frac{\partial N_i}{\partial z} & 0 & \frac{\partial N_i}{\partial x} \\ \frac{\partial N_i}{\partial y} & \frac{\partial N_i}{\partial x} & 0 \end{bmatrix}, \tag{10}$$

where N_i ($i = 1,..,8$) is the ith shape function.

3.2. Isoparametric finite elements

The finite elements reconstructed from MRI images have irregular geometry. We used isoparametric finite elements to map each element to a regular geometry element (Fig. 5).

The transformation is expressed in terms of shape functions:

$$\begin{aligned} x &= \sum_{i=1}^{n} N_i(\xi,\zeta,\eta) x_i, \\ y &= \sum_{i=1}^{n} N_i(\xi,\zeta,\eta) y_i, \\ z &= \sum_{i=1}^{n} N_i(\xi,\zeta,\eta) z_i, \end{aligned} \tag{11}$$

where (x_i, y_i, z_i) is the position of the ith node in the element numbering system. The shape functions, N_i, depend on the node's local coordinates. By using the chain rule of derivatives, we get the shape functions' derivatives relation between local coordinates and global coordinates as

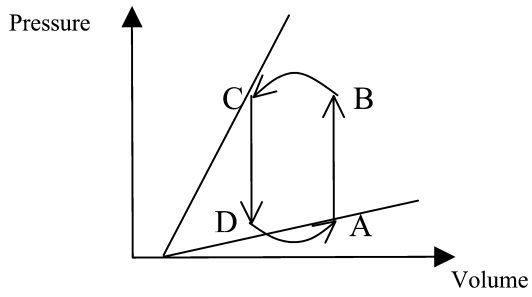

Fig. 6. Schematic ventricle pressure-volume loop, please see the text for A,B,C,D.

$$\begin{bmatrix} \frac{\partial N_i}{\partial \xi} \\ \frac{\partial N_i}{\partial \zeta} \\ \frac{\partial N_i}{\partial \eta} \end{bmatrix} = \begin{bmatrix} \frac{\partial x}{\partial \xi} & \frac{\partial y}{\partial \xi} & \frac{\partial z}{\partial \xi} \\ \frac{\partial x}{\partial \zeta} & \frac{\partial y}{\partial \zeta} & \frac{\partial z}{\partial \zeta} \\ \frac{\partial x}{\partial \eta} & \frac{\partial y}{\partial \eta} & \frac{\partial z}{\partial \eta} \end{bmatrix} \begin{bmatrix} \frac{\partial N_i}{\partial x} \\ \frac{\partial N_i}{\partial y} \\ \frac{\partial N_i}{\partial z} \end{bmatrix} = J \begin{bmatrix} \frac{\partial N_i}{\partial x} \\ \frac{\partial N_i}{\partial y} \\ \frac{\partial N_i}{\partial z} \end{bmatrix}, \quad (12)$$

where J is called the Jacobian matrix. The Jacobian of the transformation will determine whether the material is incompressible.

If a local coordinate system is defined on $\xi,\zeta,\eta \in [-1,1]$, and boundary pressure is acting on face $\xi,\zeta \in [-1,1]$, $\eta = 1$, then K^e, P^e_{p}, and P^e_{a} can be easily calculated as

$$\begin{aligned} K^e &= \int_{-1}^{1}\int_{-1}^{1}\int_{-1}^{1} B^{\mathrm{T}} D B |J| \mathrm{d}\xi\, \mathrm{d}\zeta\, \mathrm{d}\eta, \\ P^e_{\mathrm{p}} &= \int_{-1}^{1}\int_{-1}^{1} N^{\mathrm{T}} f_p |J| \mathrm{d}\xi\, \mathrm{d}\zeta, \\ P^e_{\mathrm{a}} &= \int_{-1}^{1}\int_{-1}^{1}\int_{-1}^{1} N^{\mathrm{T}} f_{\mathrm{a}} |J| \mathrm{d}\xi\, \mathrm{d}\zeta\, \mathrm{d}\eta. \end{aligned} \quad (13)$$

3.3. Boundary conditions

In our finite element model, the principal boundary condition is the blood pressure in the two ventricular cavities, which changes over time. The left ventricle receives blood from the left atrium and pumps the blood through the aorta to the systemic circulation. As shown schematically in Figs. 6 and 7 (Glass et al., 1991; Hoppensteadt and Peskin, 2002), the mitral valve closes at A and the left ventricle undergoes isovolumic contraction with rapidly rising pressure until B, when the left ventricular pressure exceeds the aortic pressure and the aortic valve opens, blood is ejected and the left ventricle's volume begins to decrease. The aortic valve closes at end of systole at C, due to the decreasing intraventricular pressure, which falls below the aortic pressure. The left ventricle then undergoes isovolumic relaxation from C to D. The mitral valve reopens at D when the pressure of left ventricle is lower than that of left atrium. Blood pressure in the right ventricle cavity changes similarly over the heart contraction cycle, although its magnitude is smaller than that of the left ventricle. In our implementation, the heart contraction cycle was divided into 5 time steps and representative values were used for the blood pressure at each time step.

The blood pressure values used over time are given in Table 1.

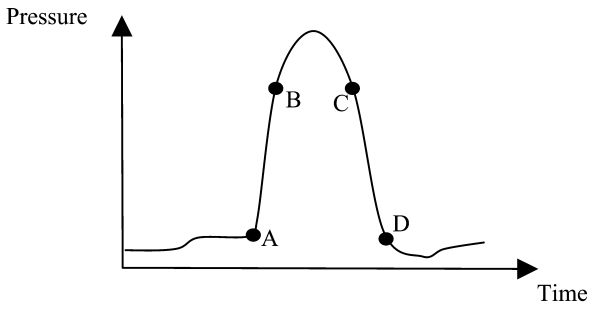

Fig. 7. Ventricle pressure changes over time, A,B,C,D are the same with Fig. 6.

3.4. Residual strain and stress

To measure the residual strain, researchers have cut cross-sectional equatorial slices from potassium-arrested rat left ventricles (Omens and Fung, 1990a,b). These were then cut radially and it was found that they immediately opened into a curved arc with an open-angle which quantified the residual strain. In our model, both the circumferential residual strain and the radial residual strain are assumed to vary linearly from the epicardium to the endocardium. We assume the circumferential residual strain is 0.05 at the epicardium and -0.05 at the endocardium, while the radial residual strain is -0.05 at the epicardium and 0.05 at the endocardium (Costa et al., 1997).

4. Statistical estimation of K and f_{a}

4.1. Expectation/maximization (EM) algorithm

In Eq. (7), the elasticity matrix D and the active force f_{a} are unknown. The in vitro elasticity parameters of canine heart have been measured (Usyk et al., 2000); we used these data as initial values because of the general similarity between human and canine hearts. We then used the Expectation/Maximization (EM) algorithm (Bickel and Doksum, 2001) to estimate the stiffness and active force at each time step. The EM algorithm is typically used to

Table 1
Blood pressure in each time step

Time	1	2	3	4	5
Normal LV (mmHg)	8.2–12.0	45.8–49.5	83.3–87.0	113.3–118.0	98.3–103.1
Normal RV (mmHg)	8.2–12.0	15.0–19.7	18.8–23.3	22.5–27.0	18.8–23.3
RVH LV (mmHg)	8.2–12.0	45.8–49.5	83.3–87.0	113.3–118.0	98.3–103.1
RVH RV (mmHg)	15.0–19.5	30.0–34.6	60.0–64.5	67.5–72.0	60.8–65.3

compute maximum likelihood estimates given incomplete samples. Define $J(\theta|\theta_0)$ as

$$J(\theta|\theta_0) \equiv \text{Expectation}_{\theta_0}\left(\log \frac{p(X,\theta)}{p(X,\theta_0)} \,\middle|\, S(X) = s \right), \qquad (14)$$

where X is the random variable, θ is the parameter to be estimated, $S(X)$ is the sufficient statistics on X, and $p(X,\theta)$ is the probability density function. The EM algorithm works as follows:

(1) Initialize $\theta_{\text{old}} = \theta_0$
(2) Compute $J(\theta|\theta_{\text{old}})$ for many values of θ
(3) Maximize $J(\theta|\theta_{\text{old}})$ as a function of θ
(4) Set $\theta_{\text{new}} = \arg\max J(\theta|\theta_{\text{old}})$, if $\theta_{\text{old}} \neq \theta_{\text{new}}$, set $\theta_{\text{old}} = \theta_{\text{new}}$ and go to step 2, otherwise, return $\theta = \theta_{\text{new}}$.

where Step 2 is often referred to as the expectation step and Step 3 is called the maximization step.

4.2. Implementation

In our study, the parameters estimated are Young's moduli along the fiber direction (E_1) and across the fiber direction (E_2), respectively, and the active force (f_a). We can denote them together as $\theta = (E_1, E_2, f_a)$. The displacement error is defined as

$$d(x,\hat{\theta}) = \frac{1}{n}\sum_{i=1}^{n}\left[(x_i - x_{it})^2 + (y_i - y_{it})^2 + (z_i - z_{it})^2\right], \qquad (15)$$

where (x_i, y_i, z_i) is the computed global coordinate based on estimate $\hat{\theta}$, and (x_{it}, y_{it}, z_{it}) is the reconstructed global coordinate from MRI tagging. Since the smaller the displacement error, the better the estimation is, we put more weight on estimations with less displacement error. Our normalized density function is then defined as

$$p(x,\hat{\theta}) = \frac{1/d(x,\hat{\theta})}{\sum_{\theta\in\Theta}(1/d(x,\theta))}. \qquad (16)$$

As shown in Fig. 3, since E_1 and E_2 are approximated as piece-wise linear, we need to estimate θ in each time interval. We assume E_1 and E_2 are linearly related. The implementation algorithm is:

(1) Initialize $t = 1$
(2) In the tth time interval, calculate $d(\theta)$ and $p(x,\theta)$ for many $\theta \in \Theta$
(3) Initialize $(E_{1,\text{old}}, E_{2,\text{old}}) = (E_{1,0}, E_{2,0})$, where $E_{1,0}$ and $E_{2,0}$ are calculated from the experimental data given in (Usyk et al., 2000)
(4) Fix $(E_{1,\text{old}}, E_{2,\text{old}})$, using the EM algorithm to get optimal estimation $f_{a,\text{new}}$
(5) Fix $f_{a,\text{new}}$, using the EM algorithm to get optimal estimation $(E_{1,\text{new}}, E_{2,\text{new}})$
(6) If $(E_{1,\text{old}}, E_{2,\text{old}}) \neq (E_{1,\text{new}}, E_{2,\text{new}})$, set $(E_{1,\text{old}}, E_{2,\text{old}}) = (E_{1,\text{new}}, E_{2,\text{new}})$, go to step 4,
otherwise, return $(E_1, E_2, f_a) = (E_{1,\text{new}}, E_{2,\text{new}}, f_{a,\text{new}})$
(7) $t = t + 1$, if $t < nt$, go to step 2, otherwise, stop.

where nt is the number of time steps.

5. Results

5.1. Finite element interpolation

For the normal heart, the model we used for the left ventricle reconstructed from MRI tagging has 264 eight-noded elements and 327 nodes while the right ventricle has 80 eight-noded elements and 146 nodes. To model the fiber orientation change from epicardium to endocardium and improve the precision of computation, each parallelepiped element was interpolated into 27 eight-noded subelements. After the interpolation, the normal heart model has 5256 eight-noded elements and 6303 nodes for the left ventricle and 1536 eight-noded elements and 2202 nodes for the right ventricle. Similarly, the model of the RVH heart model was interpolated and it has 4818 eight-noded elements and 5778 nodes for the left ventricle and 1920 eight-noded elements and 2730 nodes for the right ventricle after the interpolation.

5.2. Fiber orientation

In Fig. 8, we have shown the fibers in the epicardium and endocardium at the end of diastole. In (a), the tiny blue line in each element shows the orientation of fibers within the epicardium elements. In (b), we have shown the fiber orientations of 6 elements from epicardium to endocardium across the left ventricle wall. The fiber orientation of the endocardium is shown in (c). The fiber orientation of each element changes over time; we can compute the current fiber orientation at each time step by calculating the current coordinates of representative points on the fiber. The fiber orientation data was then plugged into Eq. (6) to compute each element's current compliance matrix.

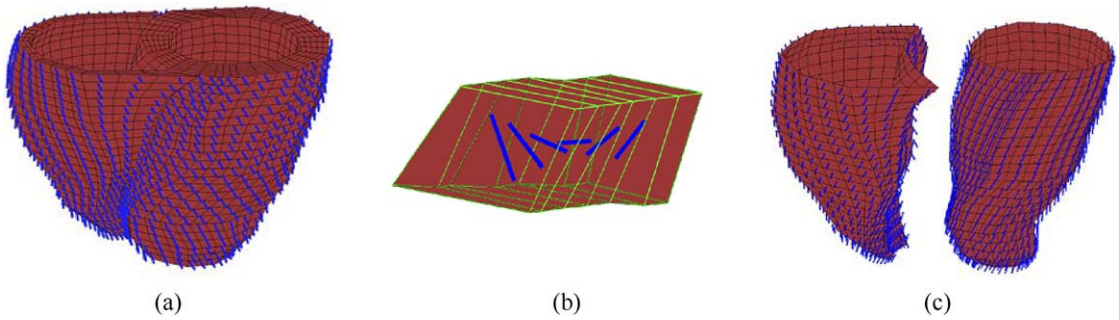

Fig. 8. Fibers of a normal heart: (a) in epicardium, (b) from epicardium(left) to endocardium(right), (c) in endocardium. (This figure is available in colour, see the on-line version.)

Table 2
Initial assignment of Young's modulus in each time interval

	Time interval	1–2	2–3	3–4	4–5
Normal	E_1 (Pa)	50 000.0	60 000.0	70 000.0	80 000.0
	E_2 (Pa)	15 000.0	18 000.0	20 000.0	22 000.0
RVH	E_1 (Pa)	60 000.0	70 000.0	80 000.0	90 000.0
	E_2 (Pa)	18 000.0	20 000.0	22 000.0	25 000.0

Table 3
Final estimation of Young's modulus in each time interval

	Time interval	1–2	2–3	3–4	4–5
Normal	E_1 (Pa)	48 300.0	59 700.0	71 200.0	77 600.0
	E_2 (Pa)	14 200.0	16 700.0	21 000.0	20 800.0
RVH	E_1 (Pa)	61 700.0	73 500.0	82 400.0	95 700.0
	E_2 (Pa)	23 500.0	24 300.0	33 300.0	36 700.0

5.3. Young's modulus estimation

The Young's moduli over one contraction cycle were initially computed from the data given in (Usyk et al., 2000) and set as shown in Table 2.

Using the statistical method described above, we get the estimation of Young's moduli in each time step as shown in Table 3.

5.4. Strain and stress distribution

The bi-ventricular strain and stress distributions of a normal volunteer and a RVH patient in one contraction cycle are shown in Figs. 9–12, respectively. In general, the ventricles become thicker radially, and shorter circumferentially and longitudinally when the heart contracts. As we can see from the images, most radial stresses are positive while most circumferential and longitudinal stresses are negative. However, some elements do not follow

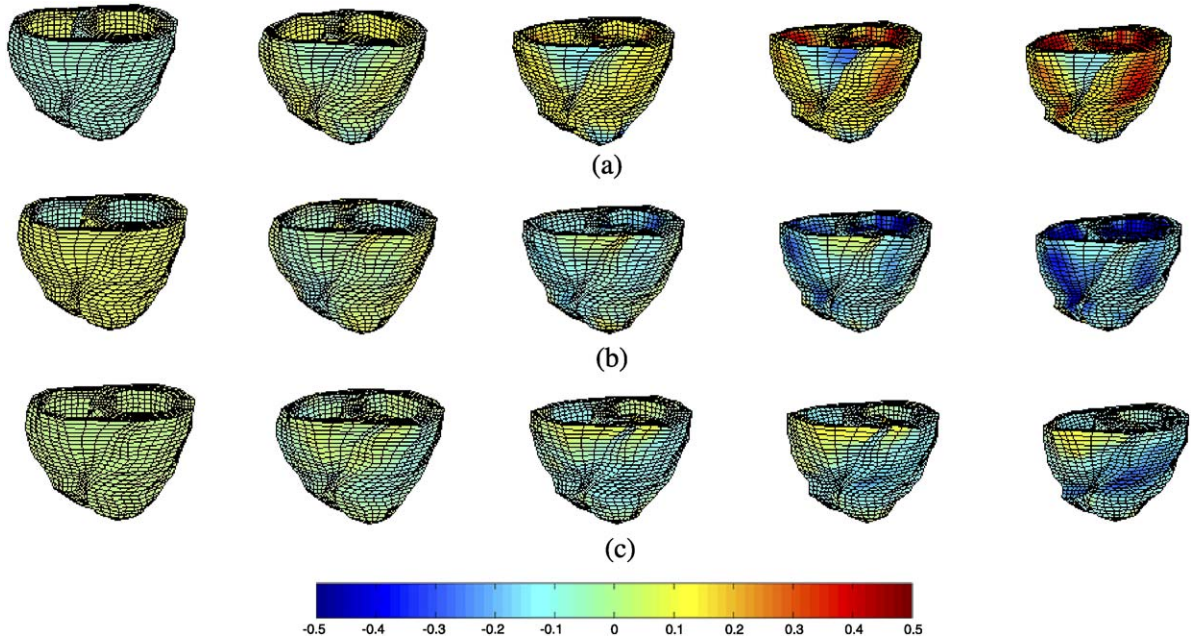

Fig. 9. Normal heart: (a) radial, (b) circumferential, (c) longitudinal components of strain from end of diastole (left) to end of systole (right). (This figure is available in colour, see the on-line version.)

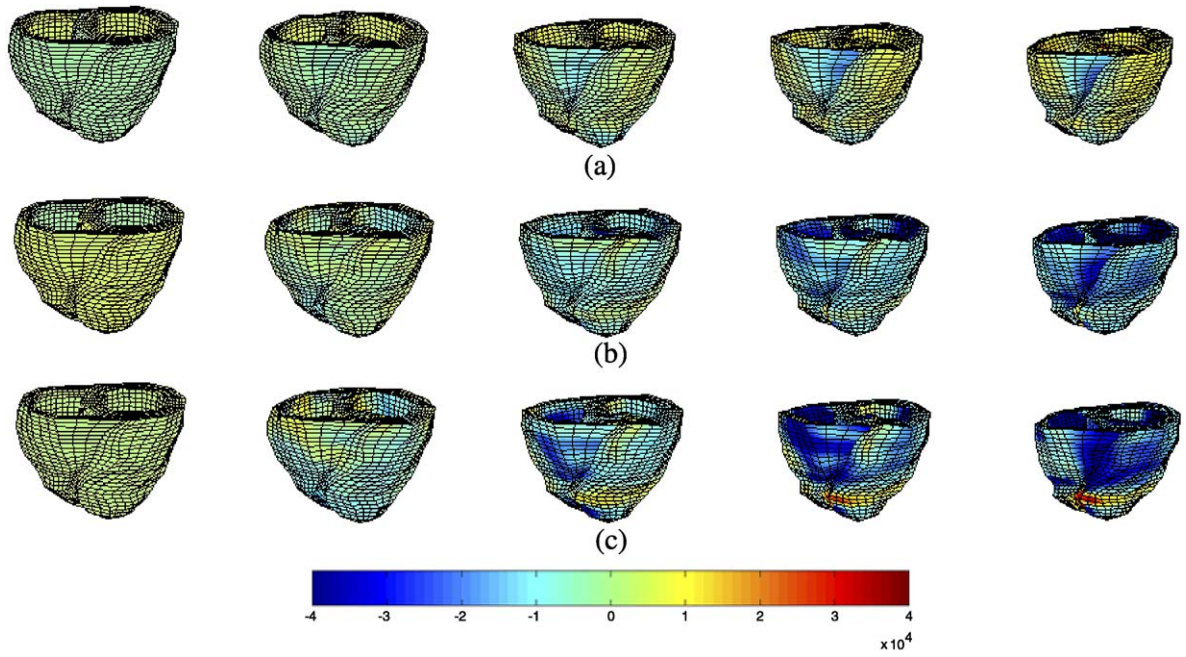

Fig. 10. Normal heart: (a) radial, (b) circumferential, (c) longitudinal components of stress from end of diastole (left) to end of systole (right). (This figure is available in colour, see the on-line version.)

this rule either because of boundary condition constraints or adjacent elements' influence.

Quantitatively, normal heart has a smoother distribution of strain and stress than abnormal heart in the-free wall. In addition, normal heart has larger strain than the abnormal heart although there is not much difference in stress between normal heart and abnormal heart. This means the normal heart deforms more than the abnormal heart, but their stresses are similar because the normal heart has smaller Young's modulus.

The numerical computation code was written in C and the output display was implemented in Matlab. The program was run on a DELL Precision 330 PC with 4 CPUs (1.5 GHz each) and 1048 MB RAM. For each time

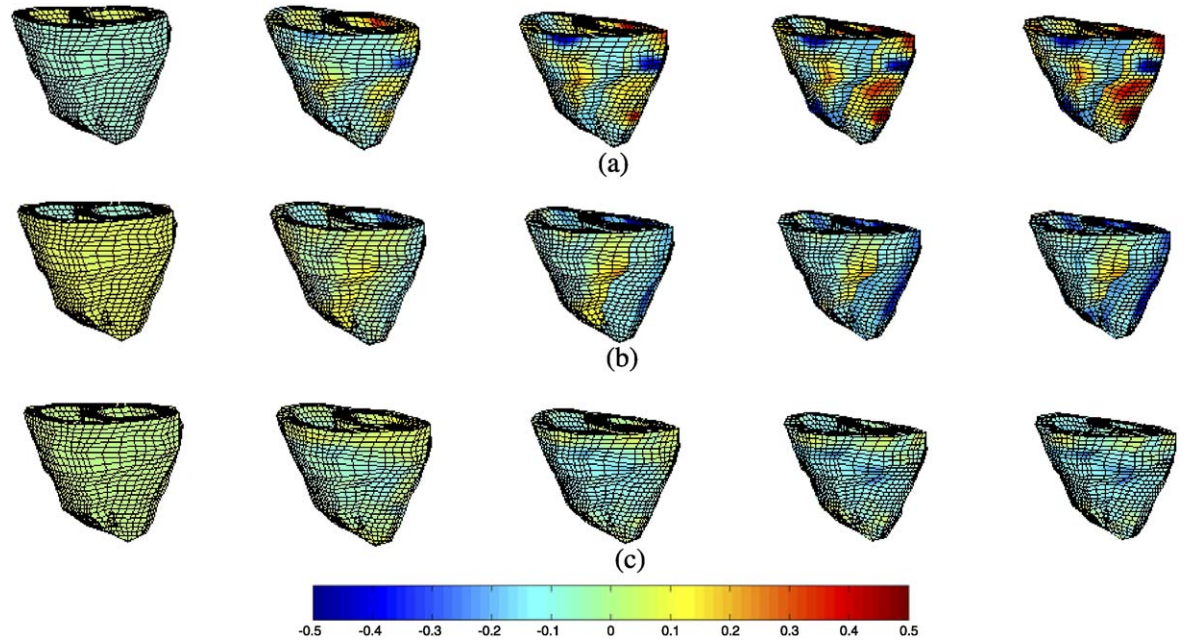

Fig. 11. RVH heart: (a) radial, (b) circumferential, (c) longitudinal components of strain from end of diastole (left) to end of systole (right). (This figure is available in colour, see the on-line version.)

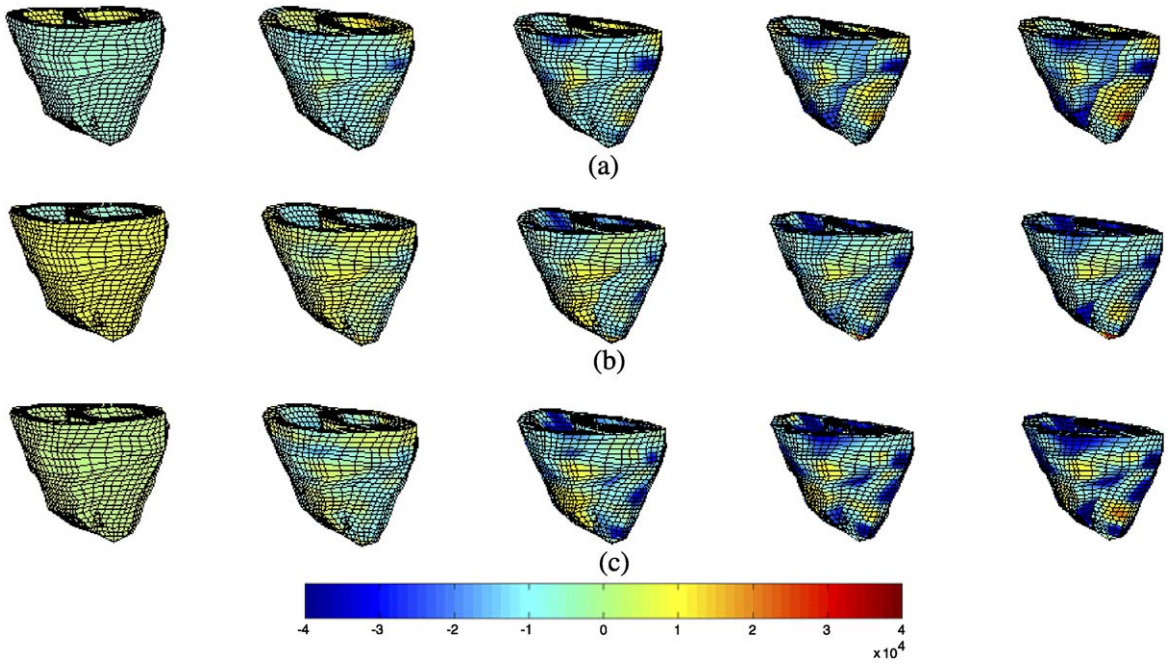

Fig. 12. RVH heart: (a) radial, (b) circumferential, (c) longitudinal components of stress from end of diastole (left) to end of systole (right). (This figure is available in colour, see the on-line version.)

step, it took around 30 min to estimate the strain and stress. The analysis for one cycle from the end of diastole to the end of systole requires around 150 min.

6. Conclusions

We have developed a novel statistical model to estimate the strain and stress of both cardiac ventricles by using accurate displacements reconstructed from MRI-SPAMM tagging and a deformable model. Compared to the traditional strain energy function method, our model gives more intuitive and understandable parameters. The results are consistent with earlier studies. They may be clinically useful in the future.

Acknowledgements

This research has been funded by grants from the NIH R01-43014.

References

Amini, A.A., Chen, Y., Curwen, R.W., Manu, V., Sun, J., 1998. Coupled B-Snake grides and constrained thin-plate splines for analysis of 2D tissue deformations from tagged MRI. IEEE Trans. Med. Imaging 17 (3), 344–356.

Axel, L., Dougherty, L., 1989. Heart wall motion: Improved method of spatial modulation of magnetization for MR imaging. Radiology 272, 349–350.

Bathe, K., 1982. Finite Element Procedures in Engineering Analysis. Prentice-Hall, Englewood Cliffs, NJ.

Bickel, P.J., Doksum, K.A., 2001. Mathematical Statistics: Basic Ideas and Selected Topics, Vol. I. Prentice Hall, Englewood Cliffs, NJ.

Caulfield, J.B., Borg, T.K., 1979. The collagen networks of the heart. Lab. Invest. 40, 364–371.

Costa, K., 1996. The Structural Basis of Three-Dimensional Ventricular Mechanics, Ph.D. Dissertation, University of California, San Diego, CA.

Costa, K., May-Newman, K., Farr, D., O'dell, W.G., McCulloch, A.D., Omens, J.H., 1997. Three-dimensional residual strain in midanterior canine left ventricle. Am. J. Physiol. 273, H1968–1976.

Demer, L.L., Yin, F.C.P., 1983. Passive biaxial properties of isolated canine myocardium. J. Physiol. 339, 615–630.

Fung, Y.C., 1984. Biodynamics: Circulation. Springer, New York.

Glass, L., Hunter, P., McCulloch, A.D., 1991. Theory of Heart: Biomechanics, Biophysics, and Nonlinear Dynamics of Cardiac Function. Springer, New York.

Guyton, A.C., Hall, J.E., 2000. Textbook of Medical Physiology, 10th Edition. W.B. Saunders, Philadelphia, PA.

Haber, I., 2000. Three dimensional motion reconstruction and analysis of the right ventricle from planar tagged MRI. Ph.D. Dissertation, University of Pennsylvania, Philadelphia, PA.

Haber, I., Metaxas, D.N., Axel, L., 2000. Three-dimensional motion reconstruction and analysis of the right ventricle using tagged MRI. Med. Image Analysis 4, 335–355.

Humphrey, J.D., Yin, F.C.P., 1987. On constitutive relations and finite deformations of passive cardiac tissue: I. A pseudostrain-energy function. J. Biomechanical Eng. 109, 298–304.

Humphrey, J.D., Yin, F.C.P., 1989. Biomechanical experiments on excised myocardium: Theoretical considerations. J. Biomechanics 22, 377–383.

Hyer, M.W., 1998. Stress Analysis of Fiber-Reinforced Composite Materials. McGraw-Hill, New York.

Hoppensteadt, F.C., Peskin, C.S., 2002. Modeling and Simulation in Medicine and the Life Sciences. Springer, Berlin.

Kaw, A.K., 1997. Mechanics of Composite Materials. CRC Press, Boca Raton, FL.

Metaxas, D.N., 1996. Physics-based Deformable Models: Applications To Computer Vision, Graphics, And Medical Imaging. Kluwer Academic Publishers, Cambridge.

Nielsen, P.M.F., LeGrice, I.J., Smaill, B.H., Hunter, P.J., 1991. Mathematical model of geometry and fibrous structure of the heart. Am. J. Physiol. 260, H1365–1378.

Omens, J.H., 1988. Left Ventricular Strain in the No-load State due to the Existence of Residual Stress. PhD thesis, University of California, La Jolla, CA.

Omens, J.H., Fung, Y.C., 1990a. Residual strain in rat left ventricle. Circ. Res. 66, 37–45.

Omens, J.H., Fung, Y.C., 1990b. Residual strain in rat left ventricle. Circ. Res. 66, 37–45.

Pao, Y.C., Nagendra, G.K., Padiyar, R., Ritman, E.L., 1980. Derivation of myocardial fiber stiffness equation on theory of laminated composite. J. Biomechanical Eng. 102, 252–257.

Papademetris, X., 2000. Estimation of 3D left ventricular deformation from medical images using biomechanical models, Ph.D. Dissertation, Yale University, New Haven, CT, May.

Papademetris, X., Sinusas, A., Dione, D.P., Duncan, J.S., 2001. Estimation of 3D left ventricular deformation from echocardiography. Med. Image Anal. 5, 17–28.

Park, J., Metaxas, D.N., Axel, L., 1996. Analysis of left ventricular wall motion based on volumetric deformable models and MRI-SPAMM. Med. Image Anal. 1, 53–71.

Pinto, J.G., Fung, Y.C., 1973. Mechanical properties of the heart muscle in the passive state. J. Biomechanics 6, 597–616.

Streeter, Jr. D.D., Hanna, W.T., 1973. Engineering mechanics for successive states in canine left ventricular myocardium: I. Cavity and wall geometry. Circulation Res. 33, 639–655.

Usyk, T.P., Mazhari, R., McCulloch, A.D., 2000. Effect of laminar orthotropic myofiber architecture on regional stress and strain in the canine left ventricle. J. Elasticity 61, 143–164.

Vetter, F.J., McCulloch, A.D., 1998. Three-dimensional analysis of regional cardiac function: a model of rabbit ventricular anatomy. Prog. Biophys. Mol. Biol. 69, 157–183.

Yin, F.C.P., Strumpf, R.K., Chew, P.H., Zeger, S.L., 1987. Quantification of the mechanical properties of non-contracting myocardium. J. Biomechanics 20, 577–589.

Young, A.A., Axel, L., Dougherty, L., Bogen, D.K., Parenteau, C.S., 1993. Validation of tagging with MR imaging to estimate material deformation. Radiology 188 (1), 101–108.